Use of non-destructive tests to explain manifested pore structure changes in cryogenic concrete

R B Kogbara[1,*], S R Iyengar[1], Z C Grasley[2], D G Zollinger[2], E A Masad[1,2]
[1] Mechanical Engineering Program, Texas A&M University at Qatar, P.O. 23874, Education City, Doha, Qatar
[2] Zachry Department of Civil Engineering, Texas A&M University, College Station, TX 77843, USA
*Corresponding author. Email: regkogbara@cantab.net

Abstract. The pore structure serves as a transport medium for external agents that cause concrete deterioration and controls the main properties of concrete. This work utilized non-destructive tests to explain pore structure changes in concrete assessed for direct liquefied natural gas (LNG) containment. It sought to investigate concrete mixture designs that are least susceptible to internal damage during cryogenic cooling. Concrete specimens were prepared using limestone and trap rock as coarse aggregates and river sand as fine aggregate. The effect of air-entrainment was also considered. Microcracking in the concrete specimens was monitored using coupled acoustic emission (AE) sensors during cryogenic cooling and warming. While proton nuclear magnetic resonance (NMR) measurements and x-ray computed tomography (XRCT) imaging were conducted on the specimens before and after the temperature swings. The manifestation of pore structure changes was assessed using water and 'chloride permeability' tests. Significant microcracking and changes in NMR porosity and mean pore size, and CT-calculated porosity corresponded to changes in water permeability trend but not 'chloride permeability' trend. Air entrainment caused a reduction in chloride penetrability. The results show the utility of the non-destructive tests in explaining pore structure changes in cryogenic concrete and identifies the damage-resistance potential of the concrete mixtures.

1. Introduction

The main properties of concrete are controlled by the pore structure, which serves as a transport medium for external agents that cause concrete deterioration. Concrete utilized for direct liquefied natural gas (LNG) must be dense, durable, nearly impermeable, and resistant to chemicals, with limited cracking. It must also be gas-tight to prevent leakage of LNG vapour, loss of product and to promote durability [1]. Thus, the expected properties of cryogenic concrete largely depend on the pore structure. Moreover, concrete degradation occurs when external agents such as water and carbon dioxide, chloride and sulphate ions penetrate the pore structure. This manifests as an increase in the permeability of water, gas and chloride ions as well as a reduction in the overall strength and stiffness of concrete [2, 3]. At cryogenic temperatures, internal stresses occur in concrete due to hydraulic pressure from ice formation leading to 9% volumetric increase and pressure resulting from the growth of ice crystals in pores and their interaction with pore walls. The movement of liquid water towards concrete pores containing ice to restore thermodynamic equilibrium also causes osmotic pressure in the pore system of cryogenic concrete. When these internal stresses exceed the tensile strength of concrete, the material cracks [2, 4,

5]. Due to the complex and time-dependent nature of the pore structure of concrete, it is important to investigate non-destructive tests that can explain such changes in cryogenic concrete.

Microcracking in concrete from internal stresses releases strain energy, some of which is converted to wave energy. The wave energy, in turn, flows through the material and is released into the air in the form of sound, which can be detected by appropriate acoustic emission (AE) sensors [6]. When the concrete undergoes freeze-thaw cycling the amount and interconnection of internal microcracks and cracks is increased leading to changes in the total porosity and pore size distribution, and hence, permeability. Such changes in the porosity and pore size distribution can be monitored by proton nuclear magnetic resonance (^{1}H NMR) [7]. The decay of proton (from water molecules) magnetization varies with different pore sizes. Hence, information on the pore size distribution can be deduced from NMR relaxation times [8]. Similarly, comparison of the ^{1}H NMR of a concrete core with that of an equivalent amount of water can provide information on the total porosity as the amount of hydrogen in the pores of concrete proton NMR can be measured by ^{1}H NMR. Further, changes in the internal microstructure of the concrete before and after cryogenic cooling can be monitored using x-ray computed tomography (XRCT). XRCT permits three-dimensional visualization of the internal microstructure of different materials and can detect cracks and microcracks in concrete [1, 9].

The transport properties of concrete are linked to the state of microcracking [10]. Hence, it makes sense to relate the aforementioned non-destructive tests to permeability changes in cryogenic concrete. However, there is a paucity of literature in that regard. This work builds on previous related studies [1, 4] and combines information from AE, NMR and XRCT microstructural investigations of concrete mixtures to explain pore structure changes after cryogenic cooling. The objective of the study was to investigate the possibility of explaining changes in the permeability of cryogenic concrete through quantification of microstructural changes with the aforementioned techniques.

2. Methodology

2.1. Concrete mixtures

Concrete mixtures were produced using two coarse aggregates with different coefficients of thermal expansion (CTE), namely, limestone (CTE ~ 4.5 µstrain/°C) and traprock (CTE ~ 9.8 µstrain/°C) [11]. The effect of air-entrainment was also considered as entrained air voids provide extra space for pore water to flow into (and freeze), thus preventing generation of large expansive stresses that damage cryogenic concrete [1]. Type I Portland cement was used for casting the 150 mm x 150 mm x 150 mm cubic specimens, with siliceous river sand as fine aggregate, for all mixtures as shown in Table 1.

Table 1. Mixture design and properties of the concrete mixtures.

Concrete mixture	Cement (kg/m^3)	Coarse aggregate (kg/m^3)	River sand fine aggregate (kg/m^3)	Water (kg/m^3)	MasterAir AE 200 (kg/m^3)	Bulk density (kg/m^3)	28-day Compressive strength (MPa)
Limestone	512	868	694	215	-	2400	54
Trap rock	512	1056	670	215	-	2550	52
Air-entrained Limestone	543	868	614	188	2.9	2415	39
Air-entrained Traprock	543	1046	591	188	2.4	2615	42

The maximum coarse aggregate size employed was 19 mm. Water/cement mass ratios of 0.35 and 0.42 were employed for the air-entrained (with 6% air content using MasterAir AE 200, *BASF*, Ohio, USA) and non-air-entrained concrete mixtures, respectively. Cores (23 mm diameter by 50 mm long) drilled from replicate 150 mm cubes for each mixture were used for the non-destructive tests (NMR, AE and XRCT), while the cubes were used for permeability tests. The mixes were designed for 28-day compressive strengths exceeding the minimum value (34.5 MPa) specified for concrete structures for

containment of refrigerated liquefied gases [12]. Pertinent details of the concrete mixtures are shown in Table 1. The specimens were cured under water until they were tested at 28 days curing age.

2.2. Cryogenic cooling and warming of concrete specimens

The moist concrete specimens (cubes and cores) were placed in a temperature chamber (*Cincinnati Sub Zero*, Ohio, USA) and cooled to cryogenic temperatures via liquid nitrogen injection. The highest possible ramp rate of 3°C/min, which the temperature chamber could readily accommodate, was employed for cooling the specimens. This was to ensure pore structure changes occur in the different mixtures via microcracking. The cooling program was turned off after the average temperature of all concrete specimens were ≤ -165°C (i.e. below LNG liquefaction temperature). The specimens were then warmed back to ambient temperature using a single set point of 21°C (without a ramp rate program) since the study focused on cryogenic concrete and most LNG tanks in practice do not undergo thermal cycling [5]. The temperature of the concrete specimens were monitored throughout the process using Type T thermocouples placed at abraded surfaces and also inserted into the specimens and connected to data loggers (*Onset Computer Corporation*, Massachusetts and *Supco*, New Jersey, USA).

Replicate cubes and cores were used for the different tests described subsequently. Hence, they were treated differently at some point. AE sensors were placed on cubic specimens during the cooling and warming process. After warming to ambient temperature, cores for NMR measurements were re-saturated with water, while those for XRCT imaging were air-dried for tests after cryogenic cooling.

2.3. AE testing

Pancom P15 sensors with 150 kHz resonant frequency were coupled to abraded areas on the top of two cubic concrete specimens from the different mixtures using a high vacuum sealing compound, HIVAC-G (*Shin Etsu*, Japan). The body material of the sensor is nickel-plated brass; its detection element is made of PZT - lead zirconate titanate and the temperature can be taken down to -200°C. The sensors provided AE hits to AEP4 preamplifiers attached to a Vallen AMSY-6 multichannel AE measurement system (*Vallen Systeme GmbH*, Germany). The AE measurement system monitored microcracking accumulation (AE events) during the cooling and warming process. A threshold of 34 dB was used and the sampling rate was 10 MHz. The AE data for the four concrete mixtures were from the same sensor to ensure the accuracy of the results. Hence, the second sensor was coupled to a specimen not from the mixture of interest in a given cooling experiment for use in noise filtering. Thereafter, data processing was conducted using a Mathematica algorithm (Version 10, *Wolfram Research*, USA), which included filtering out noise generated during operation of the temperature chamber. Noise filtration entailed discarding data detected by both sensors at the same second as the probability that both specimens will crack at the same instant is extremely low and both sensors will detect ambient noise simultaneously.

2.4. NMR measurements

NMR measurements were performed using a 2 MHz rock core analyzer using a 54 mm probe (*Magritek*, New Zealand). The equipment generates radio frequency signals or echoes from a saturated core placed in a magnetic field. The initial amplitude of the signal indicates the total amount of fluid in the core from which the total porosity can be determined. The signal amplitude decays away with one or more relaxation times (T_2) that are characteristic of the environment of the fluid. This provides information about the pore size distribution of the core. A water-saturated concrete core was covered with plastic cling wrap to prevent moisture loss and measured using the rock core analyzer. The instrument was calibrated with 20 ml of tap water and corrected for background signal. The T_2 relaxation data was measured using the Carr-Purcell-Meiboom-Gill (CPMG) sequence with 100 μs echo time, an inter-experimental delay time of 6,500 ms and 200 scans. The T_2 of bulk water was found to be ~ 3,000 ms. The CPMG decay was then analyzed with a Lawson and Hanson non-negative least square fit method using Prospa software (*Magritek*, New Zealand). A suitable smoothing parameter was chosen to ensure a chi-squared value close to the ideal value specified by the data and well-fitted residual and data-noise statistics and residuals curves as shown in the screenshot in figure 1. The software then outputs the T_2 log-mean (a proxy for the mean pore size) in the command line history field.

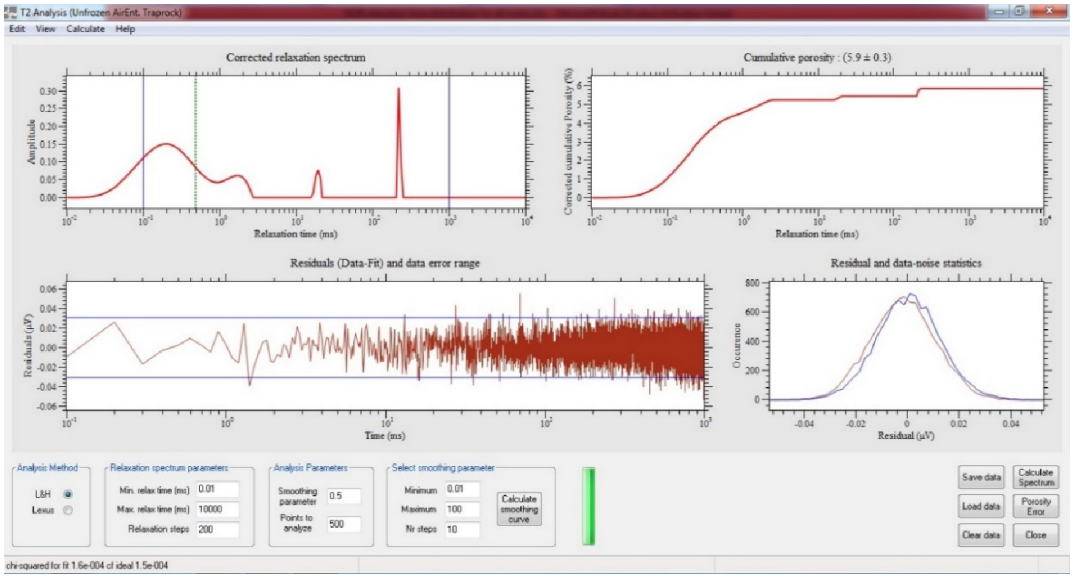

Figure 1. Screenshot of T_2 relaxation data analysis with Prospa software.

2.5. XRCT investigation

Concrete cores were scanned using a MicroXCT-400 equipment (*Carl Zeiss Microscopy GmbH*, Germany). A maximum electron acceleration energy of 140 kV was used alongside a Macro-70 (0.4X) detector and a HE #1 filter for the acquisition of 2500 projection images for each concrete mixture. The detector-rotating axis (RA) distance was 28.3 mm, while the x-ray source-RA distance was 120 mm. Post-acquisition image processing was done using Octopus Analysis software (*XRE*, Belgium). The Load Volume tool was used to load all the raw 16-bit XRCT output data into the software. These were then rescaled to 8-bit images. The images were filtered using a median filter with 26 neighborhood kernel size. Thereafter, thresholding was then used to isolate the void space (air void or crack) from the aggregates and mortar matrix. The total porosity was then deduced from the partial porosity in all (x, y and z) directions calculated using the software's analysis tool.

2.6. *Water and rapid chloride permeability tests*

Water permeability was determined on concrete cubes using the depth of penetration technique [13], which is suitable for concretes with very low permeability. A water pressure of 0.5 MPa was applied to the concrete cube during the 72-hour test duration. Thereafter, the mass of the concrete cube and the depth of water penetration were determined. These were then used to calculate the water permeability based on Valenta's equation as detailed in a related paper [4]. Cylindrical cores (102 mm diameter by 51 mm long) were extracted from the concrete cubes before and after freezing and used for the rapid chloride permeability tests following ASTM C 1202 [14]. Integration of current over time duration was used to obtain the total charge (in coulombs) passed through the concrete during a 6-hour period.

3. Results and discussion

3.1. AE monitoring of microcrack accumulation

The cumulative energy of the concrete mixtures is shown alongside the concrete temperature in figure 2. The cumulative energy can be related physically to damage growth as a large increase in cumulative energy could imply high damage growth rate during cooling [11]. The limestone mixtures showed higher (16 and 290 nJ, figure 2a) cumulative energies than the traprock (7 and 8 nJ) mixtures (figure 2b). The cumulative energy of the mixtures continued to increase down to cryogenic temperatures and reached a plateau upon warming to ambient temperature with a slight increase when warming began. This agrees with the position that matrix stresses and microcraking tendency decline significantly as concrete approaches cryogenic temperatures [1, 11]. The results show that air-entrainment led to more tendency for microcracking for the limestone mixture but had a marginal positive effect on the traprock mixture.

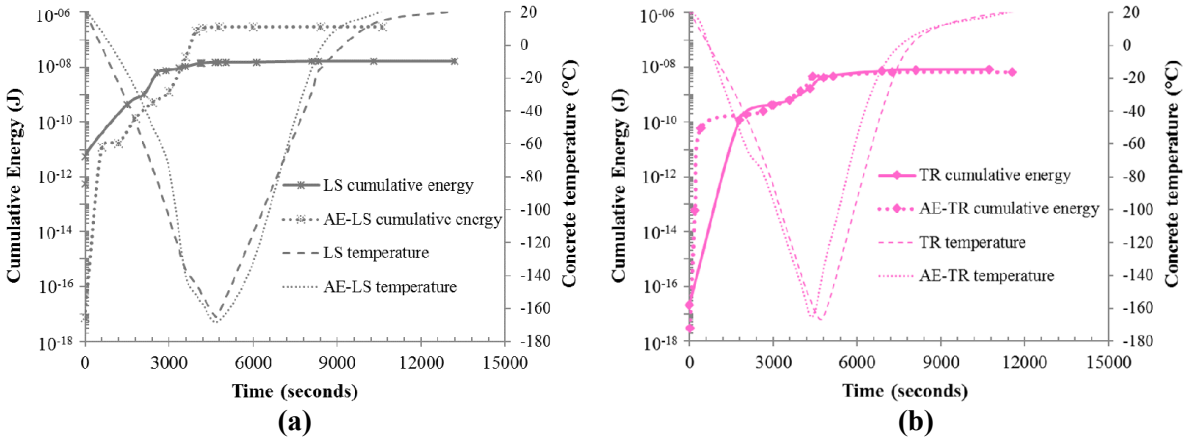

Figure 2. AE Cumulative energy of the (a) limestone and (b) trap rock mixtures, with and without air-entrainment. *Note: LS – limestone, TR – traprock, AE - air-entrained.*

3.2. NMR porosity and pore size distribution determination

Figure 3 shows the T_2 distributions and the cumulative porosities of the concrete mixtures. The peaks in figures 3a and 3b denote pores of different sizes. While the amplitude of the peaks denotes pore volume. The gel and capillary pores of the concrete mixtures are represented by the first and second peaks, which are present in all mixtures. Subsequent peaks denote larger (or very large) pores and cracks. The apparent lower porosities of the air-entrained mixtures in contrast to expected higher porosities from air-entrainment is probably due to incomplete saturation of entrained air bubbles [1].

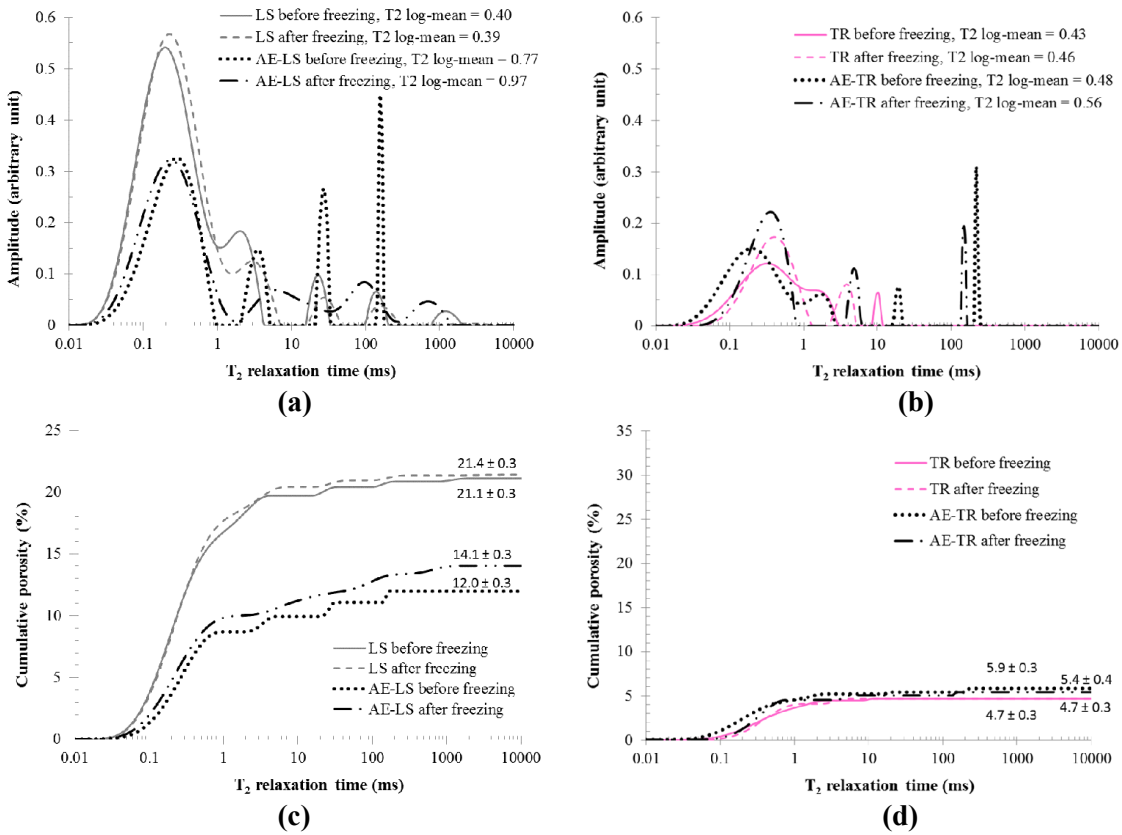

Figure 3. T2 distribution and cumulative porosity, respectively, of the (a) and (c) limestone, and (b) and (d) traprock mixtures. *Note: LS – limestone, TR – traprock, AE - air-entrained.*

The log-mean T_2 values (represents mean pore size) shown in figures 3a and 3b indicate that there was no significant change in the pore size distribution of the limestone and trap rock mixtures without air-entrainment. This is supported by the cumulative porosity data. There was a slight change in the pore size distribution of the air-entrained traprock mixture as indicated by a 0.08 ms increase in the log-mean T_2 value (figure 3b). Albeit, there was no increase in the cumulative porosity but rather an apparent decrease within the error margin (figure 3d). However, the air-entrained limestone mixture showed increases in the mean pore size as indicated by increases in the log-mean T_2 and porosity by 0.2 ms (figure 3a) and 2.1% (figure 3c), respectively.

3.3. XRCT microstructural examination

The CT data set generated for each concrete core consists of 1014 slices of reconstructed images, each of which has a thickness of ~ 50 microns. The images have a matrix size of 1024 x 1024 pixels with a resolution of 22 microns per pixel in the x-y plane. Figure 5 shows an example CT scan of slice number 507 of the air-entrained limestone core processed with Octopus Analysis software. In figures 5a, 5b and 5c, air voids and cracks appear as black or very dark with the air voids being spherical in shape. The patches with bright gray shades are the aggregates, while the surrounding cementitious matrix appears with dark gray shades. Figures 5d, 5e and 5f show visualization of the voids in the x-, y- and z-directions after processing for porosity analysis.

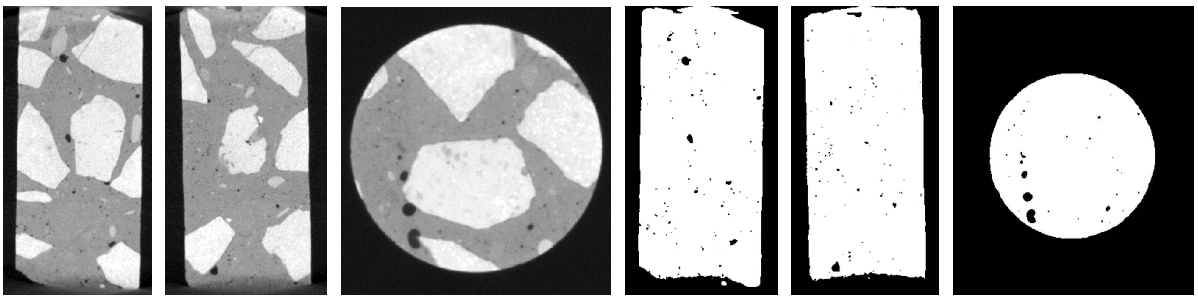

(a) (b) (c) (d) (e) (f)

Figure 4. Example CT scan showing the middle slice of the unfrozen air-entrained limestone core in the x-, y- and z-directions, respectively, in (a – c) grayscale, and (d – f) after thresholding for the void space.

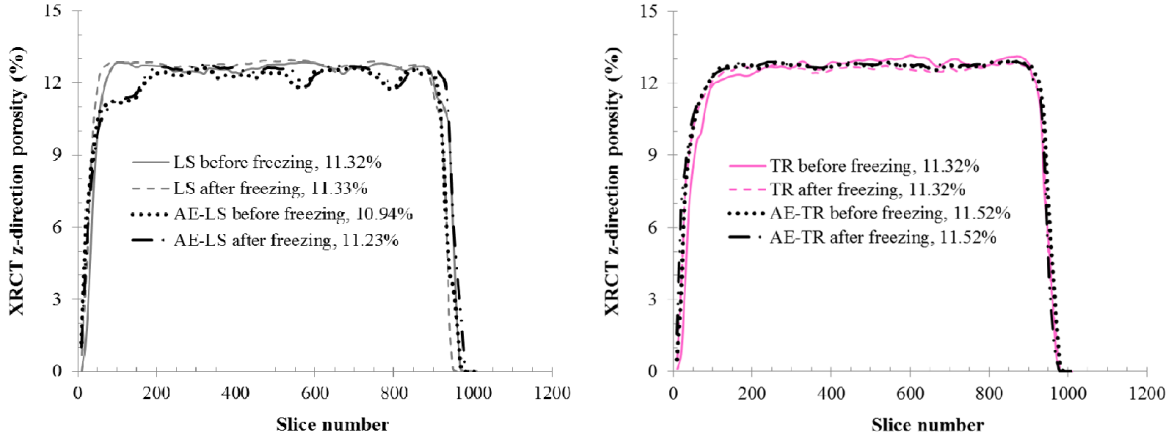

(a) (b)

Figure 5. Calculated partial porosity in the z-direction from CT images of the (a) limestone, and (b) traprock mixtures. Note: The total porosity (average in all directions) is indicated in the legends.

The porosity data of the different concrete mixtures from 2D analysis of the slices from top to bottom through the sample is shown in figure 5. The same analysis was done in the x- and y-directions to obtain the total porosities (similar in all directions) indicated in the figure legends. Interestingly, the total porosities calculated from the CT images are different from the NMR-determined porosities and similar

for all concrete mixtures. Both methods are characterized by different resolutions and the resulting porosity depends on the resolution [15]. However, there is an agreement between both methods in the total porosity change trend after cryogenic cooling as only the air-entrained limestone mixture showed a noticeable (~ 0.3%) porosity increase in the CT method (figure 5a).

3.4. Water permeability and chloride penetration resistance

Figures 6a and 6b show the water permeability and chloride penetration resistance (based on total charge passed), respectively, for the four concrete mixtures before and after cryogenic cooling. There were slight increases in the water permeability of all mixtures. The differences in permeability before and after freezing were less than half an order of magnitude, which is within the normal variability of replicate specimens [16]. The permeabilities before and after freezing differ by factors of 1.3 and 2.6 for the non-air-entrained traprock and limestone mixtures, and 2.9 and 3.2 for the air-entrained traprock and limestone mixtures, respectively. The permeability change trend is similar to the NMR and CT porosity trend, especially when the NMR porosity and pore size distribution are considered together.

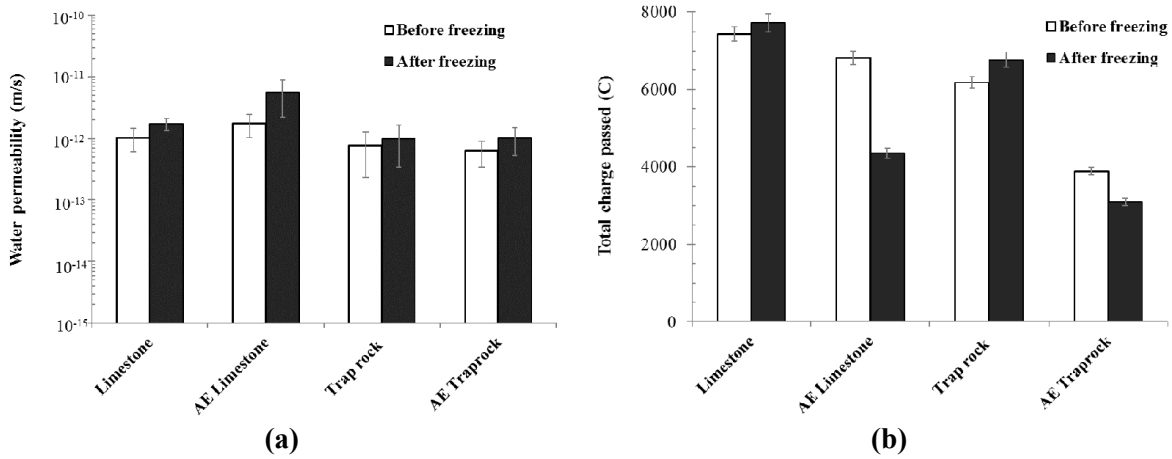

Figure 6. (a) Water permeability and (b) chloride penetration resistance of the concrete mixtures.

In the chloride penetration resistance data (figure 6b), a lower total charge passed indicates higher resistance against chloride. Figure 6b shows that air-entrainment reduced chloride ion penetrability in the limestone and traprock concrete mixtures. Interestingly, while 'chloride permeability' increased in the non-air-entrained mixtures after cryogenic cooling, it decreased in the air-entrained mixtures. The decrease after freezing was higher in the air-entrained limestone mixture. This supports the position that optimum air-entrainment enhances discontinuity of pores thereby enhancing chloride penetration resistance [17]. Overall, 'chloride permeability' did not correlate with the pore structure changes determined by AE, NMR and CT as the test actually measures ionic movement rather than permeability.

4. Conclusions

This work attempted to relate pore structure changes in four concrete mixtures determined by non-destructive techniques (AE, NMR and XRCT) to its manifestation via water and 'chloride permeability'. The results showed that significant microcracking and changes in NMR porosity and mean pore size, and CT-calculated porosity corresponded to changes in water permeability trend but not 'chloride permeability' trend. Air entrainment caused reduction in chloride penetrability. The susceptibility of the mixtures to internal damage during cryogenic cooling was in the order, non-air-entrained traprock ≥ air-entrained traprock ≥ non-air-entrained limestone > air-entrained limestone. The results show the utility of the non-destructive tests in explaining pore structure changes in cryogenic concrete.

Acknowledgements

This publication was made possible by the NPRP award (NPRP9-448-2-176: Constitutive modelling and investigation of bond-slip relationship in concrete for direct liquefied natural gas containment) from

the Qatar National Research Fund (a member of the Qatar Foundation). The statements made herein are solely the responsibility of the authors.

References

[1] Kogbara R B, Iyengar S R, Grasley Z, Masad E A and Zollinger D G 2015 Non-destructive evaluation of concrete mixtures for direct LNG containment *Mater Des* **82** 260-72
[2] Kogbara R B, Iyengar S R, Grasley Z C, Rahman S, Masad E A and Zollinger D G 2014 Relating damage evolution of concrete cooled to cryogenic temperatures to permeability *Cryogenics* **64** 21-8
[3] Yang Z, Weiss W J and Olek J 2004 Interaction between micro-cracking, cracking, and reduced durability of concrete: Developing methods for considering cumulative damage in life-cycle modeling. Publication FHWA/IN/JTRP-2004/10. Joint Transportation Research Program, Indiana Department of Transportation and Purdue University. doi: 10.5703/1288284313255.
[4] Kogbara R B, Parsaei B, Iyengar S R, Grasley Z C, Masad E A and Zollinger D G 2014 Evaluating damage potential of cryogenic concrete using acoustic emission sensors and permeability testing. In: *Proc. SPIE, Vol. 9061: Sensors and Smart Structures Technologies for Civil, Mechanical, and Aerospace Systems*, *90613B; doi: 10.1117/12.2045708*, ed J P Lynch, *et al*. (Bellingham, WA: SPIE)
[5] Krstulovic-Opara N 2007 Liquefied natural gas storage: Material behavior of concrete at cryogenic temperatures *ACI Mater J* **104** 297-306
[6] Sagar R V and Prasad B K R 2012 A review of recent developments in parametric based acoustic emission techniques applied to concrete structures *Nondestruct Test Eva* **27** 47-68
[7] Blümich B, Perlo J and Casanova F 2008 Mobile single-sided NMR *Prog Nucl Mag Res Sp.* **52** 197-269
[8] Stingaciu L R, Weihermüller L, Haber-Pohlmeier S, Stapf S, Vereecken H and Pohlmeier A 2010 Determination of pore size distribution and hydraulic properties using nuclear magnetic resonance relaxometry: A comparative study of laboratory methods *Water Resour Res* **46** W11510, doi:10.1029/2009WR008686
[9] Cnudde V and Boone M N 2013 High-resolution x-ray computed tomography in geosciences: A review of the current technology and applications *Earth-Sci Rev* **123** 1-17
[10] Alhassani Y, Bascoul A and Ringot E 1995 Microcrack study of cement-based materials by means of image analysis. In: Proceedings of the 1994 Materials Research Society Fall Meeting, 370, pp 43-8, (Boston, MA: MRS)
[11] Kogbara R B, Iyengar S R, Grasley Z C, Rahman S, Masad E A and Zollinger D G 2016 Correlation between thermal deformation and microcracking in concrete during cryogenic cooling *NDT & E Int* **77** 1-10
[12] ACI 2011 ACI 376 - Code requirements for design and construction of concrete structures for the containment of refrigerated liquefied gases and commentary. An ACI Standard. (Farmington Hills, MI: American Concrete Institute)
[13] BSI 2009 BS EN 12390-8. Testing hardened concrete. Depth of penetration of water under pressure. (London: British Standards Institution)
[14] ASTM 2006 C 1202. Standard test method for electrical indication of chloride's ability to resist chloride. (West Conshohocken, PA: ASTM International), doi: 10.1520/C1202-05
[15] Zhang Z, Kruschwitz S, Weller A, Halisch M and Prinz C 2017 Enhanced pore space analysis by use of μ-CT, MIP, NMR, and SIP. *Paper presentation at the International Symposium of the Society of Core Analysts*, Vienna, Austria, 27 August – 1 September. Paper ID: SCA2017-086.
[16] Kogbara R B, Al-Tabbaa A and Stegemann J A 2014 Comparisons of operating envelopes for contaminated soil stabilised/solidified with different cementitious binders *Environ Sci Pollut Res* **21** 3395-414
[17] Li D, Peng Z, Wenchao G, Zhengzheng D and Tiejun Z 2017 The resistance of chloride ion penetration and the microstructure of air-entrained concrete. *International Conference on Transportation Infrastructure and Materials, Qingdao, China, DEStech Transactions on Materials Science and Engineering*, doi: 10.12783/dtmse/ictim2017/9930.